Investigation of the Static Pressure Drop and Production that Occurs due to Flow Patterns in a Perforated Horizontal Wellbore

HASANAIN J. KAREEM[1], HASRIL HASINI[1], MOHAMMAD A.ABDULWAHID[2]
[1]Mechanical Engineering,
University Tenaga Nasional,
MALAYSIA

[2]Thermal Mechanical Engineering,
Southern Technical University,
IRAQ

Abstract: - This study examined the intricate interaction between flow patterns and production within a perforated horizontal wellbore. The study precisely assessed the behavior of static pressure drop by utilizing an array of flow regimes encompassing bubble, dispersed bubble, transitional bubble/slug, slug, stratified, transitional slug/stratified wave, and stratified wave. Remarkably, an upward trend in static pressure drop was observed with increasing water phase presence, while the converse was true for the air phase. Besides, the air phase superficial velocity exhibited a direct correlation with the magnitude of pressure drop fluctuations. The liquid production demonstrated a peak during bubble and slug flow regimes, followed by a descent during the transition to stratified and stratified wave flow. This decline can be attributed to mixing pressure drops localized during the perforations. Furthermore, an upward trend in average liquid production was observed with increasing mixture superficial velocity, primarily due to the dominant presence of the water phase. Additionally, the percentage of liquid production was positively associated with the water's superficial velocity when the air's superficial velocity was held constant. While the experimental and numerical results were in agreement for slugs and structured flows, there were discrepancies in the behavior of static pressure for bubbles, small bubbles, and structured waves.

Key-Words: - flow patterns, static pressure drop, production optimization, multiphase flow, experimental and numerical analysis, perforated horizontal wellbore.

Received: June 11, 2023. Revised: February 23, 2024. Accepted: April 5, 2024. Published: May 28, 2024.

1 Introduction

Perforated horizontal pipes were significantly utilized in different sectors, ranging from water, oil, and air to water treatment and chemical engineering applications. It is for this reason that knowledge of the flow governing mechanisms inside these perforated horizontal wellbores was considered paramount to production optimization. One of the primary areas researchers focused on was the flow patterns developed due to changes in surface velocities of water and air inside these wellbores—as these patterns directly led to pressure drop effects along their lengths, consequently hampering output procedures.

Several investigators in perforated horizontal wellbores have taken up the flow patterns and pressure gradient research. Flow patterns and pressure gradients in horizontal pipes were studied by [1] and [2] who found that larger pressure gradients are associated with higher oil and water surface velocities; this indicated observation of the variations of the pipe's pressure gradient which changed when the flow regime transitions were done alongside with decreasing diameters of pipes as a mechanism to increase pressure gradients.

The past studies considered particular flow patterns. For instance, [3], delved into the impact of slug flow patterns in horizontal pipes on pressure drop and velocity profiles. In a different approach, [4], identified stratified flow patterns in horizontal pipes where air accumulated at the top and water at the bottom without bubbles. Meanwhile, [5], explored scattered bubbles, stratified, and slug flow in horizontal pipes as part of their study. Similarly, [6], investigated slug flow patterns and made an interesting observation that an increase in liquid

flow rate results in a higher liquid holdup even when gas flow is kept constant.

[7], investigated slug flow patterns and pressure drop fluctuations associated with slug formation. Bubble generation was noted when the superficial water velocity exceeded the superficial air velocity. [8], [9], [10], [11] and [12], investigated bubble formation due to shear stress forces and discovered that bubble size increased with longer horizontal pipe lengths. [13], studied stratified wavy, slug, and annular flow patterns in a horizontal pipe and found an increase in wave size while transitioning from stratified wave flow to slug flow. [14], demonstrated connections between increased pressure drop and both increased gas-liquid two-phase flow rate and higher perforation density. [15], studied bubble flow patterns, observing an increase in pressure drop with increasing liquid flow rate.

[16], moreover, demonstrated a gradual increase in total and friction pressure drops with increasing wellbore length, with a lesser impact on mixing and acceleration pressure drops. [17], attributed increased pressure loss with increasing liquid flow rate to friction loss. [18], observed bubble accumulation at the upper pipe section due to buoyancy forces and an increase in wave size with pipe length. [19], explained that an increased mass flow rate within the horizontal wellbore led to an increase in pressure drop.

[20], found that pressure drop was higher in perforated horizontal wellbores with a 90º angle phase compared to those with 0º and 180º angle phases due to the increased influence of mixing pressure drop on increasing swirling. [21], observed that liquid holdup increased when the liquid flow rate increased, and they also noticed that the max flux and pressure drop increased at an increased liquid holdup fraction. [22], investigated flow patterns and pressure drop in the horizontal pipe and observed that the stratified flow pattern was obtained through the horizontal pipe only when the liquid flow was located at the bottom wall, while gas flowed at the upper wall of the horizontal pipe. They noted that the pressure drop increased by increasing the liquid flow rate due to the friction force effect.

Within this work, we embark upon an experimental investigation of the flow dynamics within a perforated horizontal wellbore featuring two perforations and a phasing angle of °180. The key focus of this investigation is centered on changes taking place along the wellbore itself; these modifications encompass pressure drop, flow patterns, and production. Based on the experimental outcomes, this research aims to understand the static pressure drop behavior exhibited by diverse flow patterns, namely bubble flow, transition bubble/dispersed bubble flow, transition bubble/slug flow, slug flow, stratified flow, transition slug/stratified wave flow, and stratified wave flow. These patterns emerge because of dissimilar superficial mixture velocities between the air and water phases. Furthermore, the influence of the friction factor is examined through an analysis of both unperforated and perforated pipes, utilizing the aforementioned experimental results.

2 Experimental Apparatus

This study utilized a perforated horizontal pipe as the primary apparatus for investigating the phenomenon under investigation (Figure 1). Two perforations are designed on a pipe in a vertical direction with an exact angle of 180°. This design was influenced by [23], work but used different specifications for the horizontal pipe perforation as well as the perforation setup.

Transparent Perspex (acrylic) is used to make the primary channel, which is 3 m long and has an internal diameter of 0.0381 m; it features two perforations with an inner diameter of 0.004 m placed at specific locations along its wall. Through the pipe's transparency, scientists can take photos to visually document flow patterns: this helps them see variances in air and water superficial velocities.

This is primarily documented visually using a high-speed camera (Vision Datum LEO720S) — as shown in Figure 2. Capable of recording at 1,000 frames per second, this camera features a resolution of 720 × 540 pixels that makes it adaptable for different flow pattern visualizations. Tailoring the recording range between 100 and 1,000 fps enables a personalized approach to gathering data specific to the flow regime being analyzed. It's an overview of the tool we use: with information about its ability and how we can adjust it to our advantage based on what we are studying.

The primary pipe initiates an axial water flow using a centrifugal pump. Instantaneously, an electro-air compressor is used to introduce a radial airflow through the perforations located along the pipe's wall. The axial water flow has superficial velocity values ranging from 0.27 to 0.55 m/s, while the radial air flow's superficial velocities range from 0.066 to 33.1 m/s, as measured by two air flow meters.

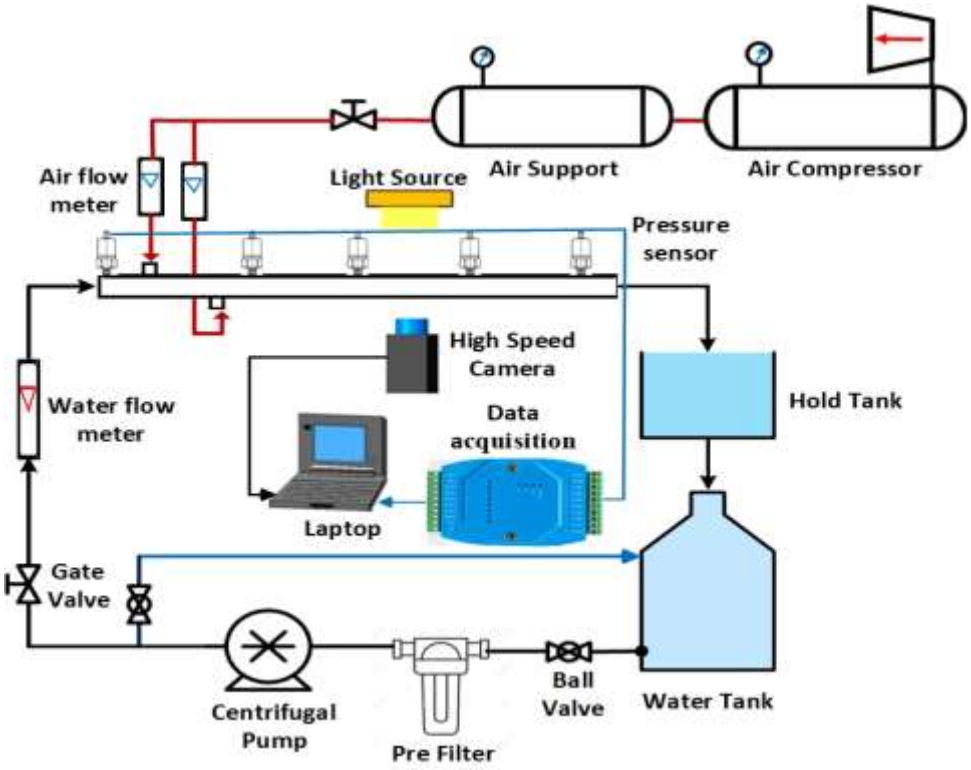

Fig. 1: Experimental Apparatus

Fig. 2: High-Speed Camera

2.1 Procedures Measurement

This study employed a series of five pressure sensors to measure the static pressure drop of a two-phase air-water flow along the perforated horizontal pipe. The pressure sensor model utilized was the WNK81mA, offering a micro pressure range of 0-20 kPa with an accuracy of 1%. These sensors, powered by a 24 V supply, produce a current output signal ranging from 4 to 20 mA (MilliAmperes). To facilitate data acquisition, an analog signal acquisition module with 1% accuracy was used to convert the 4-20 mA signal into the RS485 communication protocol, enabling connection to a laptop via a USB interface. This module is also powered by a 24 V supply, as depicted in Figure 3.

The Modbus poll software served as a master simulator, emulating a slave ID corresponding to the pressure sensor, operating at a baud rate of 9,600 bits per second. The transmission of pressure sensor data entailed receiving the signal through the data acquisition unit, which then transmitted the information to a laptop running the master Modbus software. The recorded data was stored in Microsoft Excel, as depicted in the diagram presented in Figure 4.

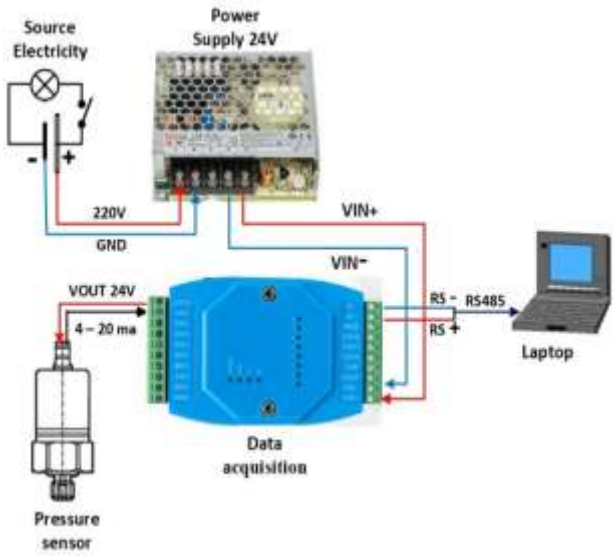

Fig. 3: The Procedure of System Connection

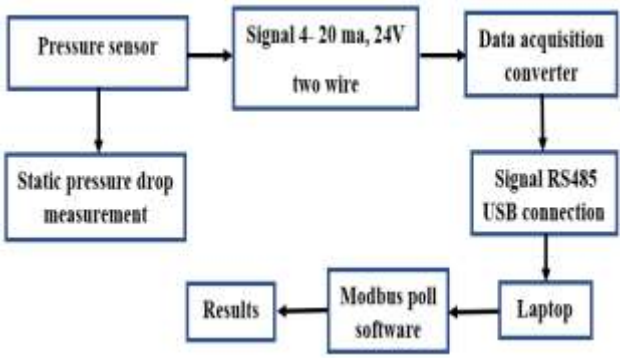

Fig. 4: Diagram of the Transmission Signal of the Sensor Pressure Transmitter

2.2 Mechanism of the Behavior of Static Pressure Drop

Experimental observations revealed an inverse relationship between the static pressure drop and the presence of the air phase.

On the contrary, the presence of the water phase demonstrated a direct correlation with the pressure drop. According to [19], increased water concentration increases the static pressure drop value. Figure 5 depicts the air-water two-phase mixture flow with varying densities and viscosities, explaining the variance in pressure sensor readings.

[19], found a positive link between the static pressure drop and the holdup fraction, which is the ratio of water volume to total mixture volume. Higher holdup fractions cause more water flow, leading to increased flow resistance. Also, found a negative link between pressure drop and void fraction, which is the percentage of air volume to total mixture volume. A higher vacancy fraction leads to less water flow and lower flow resistance.

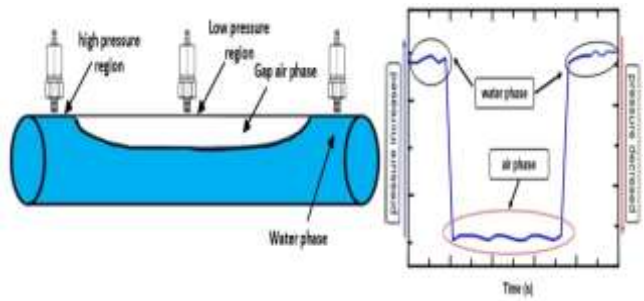

Fig. 5: Mechanism of Pressure Sensor Transmitter

2.2.1 Change in Flow Pattern with Elevated Air Superficial Velocity

Figure 6 shows how flow patterns change when air superficial velocity increases but water superficial velocity remains constant. Cases 2.1 and 2.2 show a bubble flow pattern with air dispersed inside the continuous water phase. This pattern occurs when the water's superficial velocity exceeds that of the air, influenced by shear stress, surface tension, and the differing viscosities and densities of the mixture components. As a result, the air phase separates and gathers in the upper part of the pipe due to buoyancy forces.

2.2.2 Transitional Regimes:

As air superficial velocity increases (case 2.3), the dispersed bubble flow transforms into a cloud-like dispersed bubble flow. This transition is marked by the formation of a larger concentration of non-coalescing bubbles, resembling a "cloud." Further, an increase in air velocity (case 2.4) leads to the growth and shape transformation of bubbles. While maintaining diverse sizes and shapes, the bubbles exhibit a tendency towards sphericity. Notably, a stratified/dispersed bubble flow is observed along the horizontal pipe, characterized by bubble merging, and consequently increasing bubble size and quantity.

2.2.3 Plug Flow and Stratification:

Case 2.5 presents a plug flow pattern, with elongated bubbles accumulating at the pipe's top portion. These "bullet-shaped" bubbles, formed in the fully developed flow region, result from the coalescence of smaller bubbles. Notably, this pattern appears stratified from an uphill perspective, while exhibiting a bubble flow nature from a comprehensive viewpoint. Conversely, stratified flow occurs under higher air velocities (case 2.6). This regime is characterized by air accumulating at the upper pipe section due to buoyancy, while the water phase flows downwards driven by gravity.

2.2.4 Slug Flow and Production Implications:

At even higher air superficial velocities (case 2.7), slug flow manifests with significant wave peaks. This pattern features air gaps formed by the coalescence of smaller bubbles, separated by a water layer developed in the fully developed flow region. The high airflow dynamics result in lifted water, leading to the formation of high peaks in the water waves.

It is crucial to note that bubble flow patterns persist near the bottom perforation due to the concentrated water phase and surface tension. However, case 2.8 highlights the emergence of a large air gap near the upper perforation because of high air velocity. This gap subsequently diminishes in size towards the bottom perforation. Furthermore,

the water layer separating the air gaps increases with higher air velocities, ultimately hindering the axial flow of water and potentially leading to production losses in perforated horizontal wells.

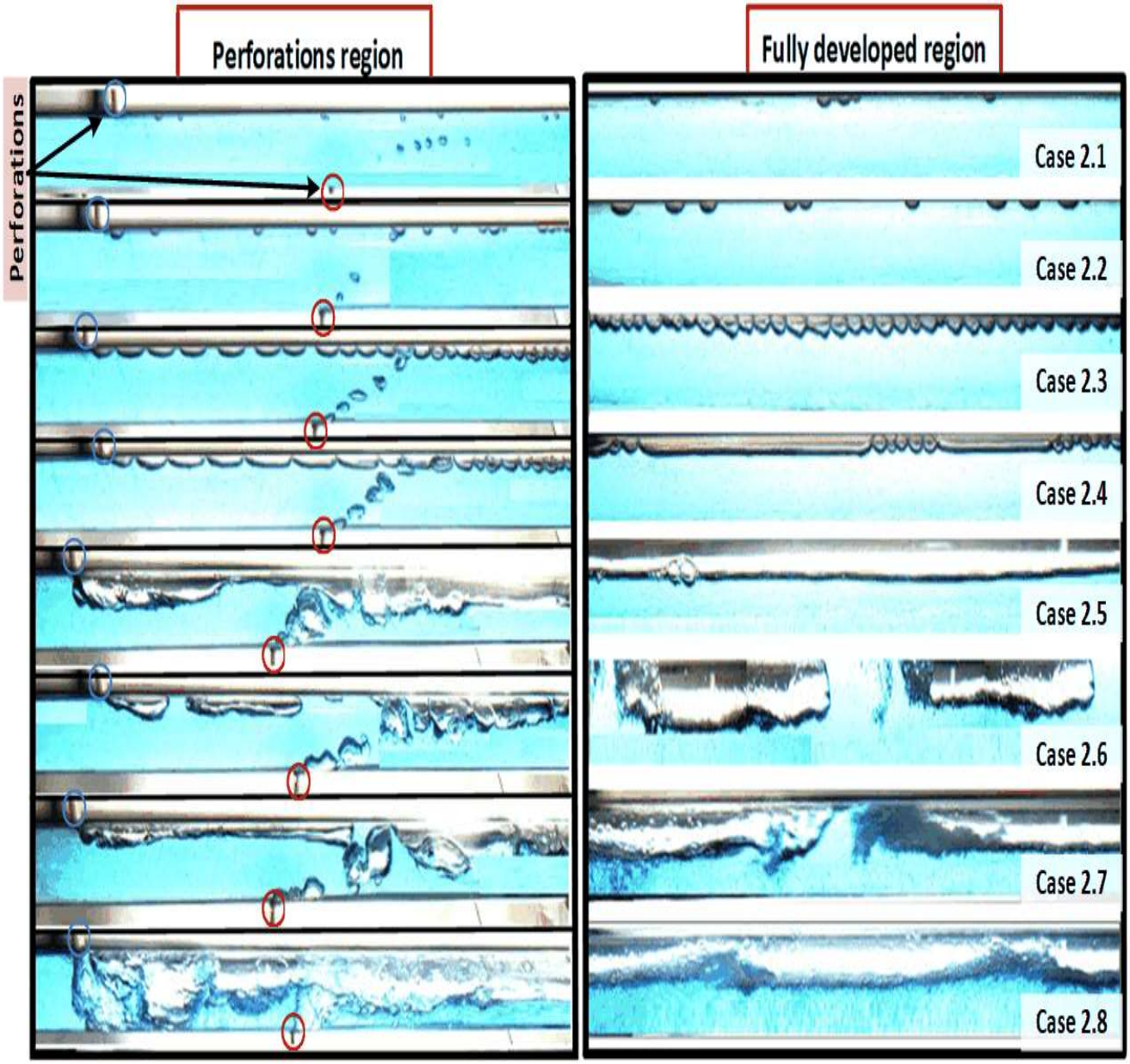

Fig. 6: Flow patterns in a horizontal perforated pipe

3 Numerical Analysis

3.1 Grid Independence Study

This study employed computational fluid dynamics (CFD) software, specifically ANSYS FLUENT R3 (2019), to generate a three-dimensional (3D) computational domain discretized using a tetrahedral mesh. The research investigated a two-phase transitional flow within a perforated horizontal pipe. The pipe had a length of 3 m, an internal diameter of 0.0381 m, and two perforations with inside diameters of 0.004 m and a phasing angle of 180°. This configuration aimed to simulate the complexities of flow encountered in horizontal wellbores.

Due to the computational demands and extended simulation run time associated with a full-scale model, a half-symmetric horizontal pipe was employed along the y-axis. The symmetric method

was implemented to ensure the preservation of flow patterns, velocity profiles, and total pressure drop within the pipe by mirroring the pipe's geometry.

To account for the viscous effects within the turbulent boundary layer near the pipe wall, a mesh sensitivity analysis was conducted. The analysis investigated four mesh sizes: 75,000 cells, 1,000,000 cells, 1,500,000 cells, and 2,000,000 cells. Each mesh configuration incorporated five inflation layers, as illustrated in Figure 7. Grid independence was established by demonstrating the consistent, regular shape of the bubble flow pattern within the perforated horizontal wellbore across different mesh sizes. Additionally, the time required for simulation convergence decreased with increasing mesh refinement.

3.2 ANSYS Fluent Analysis Procedure

This study employed the ANSYS Fluent software, utilizing the Volume of Fluid (VOF) model, to simulate the flow patterns observed within a perforated horizontal pipe. The simulations incorporated the effects of gravity due to material property discrepancies, promoting optimal flow regimes. Additionally, implicit body force treatment was implemented to ensure convergence by balancing body forces and pressure gradients within the momentum equations. To address pressure-velocity coupling skewness, the Pressure-Implicit with Splitting of Operators (PISO) method was employed. Furthermore, the Staggering Pressure Option (PRESTO) scheme, coupled with a second-order upwind scheme, was utilized to solve the momentum equations and perform pressure interpolation. Turbulent flow and near-wall mesh density treatment were achieved through the application of the Renormalization Group (RNG) and differential viscosity models, respectively.

Within this investigation, air and water were designated as the first and second phases, respectively. To facilitate the acquisition of a more accurate distribution pattern, the initial volume fraction of water within the wellbore was assumed to be 1, signifying a wellbore entirely filled with water before air introduction. The contact angle employed, which influences bubble composition, was set at 36°. This selection ensured compatibility with the interface between the air and water phases, as corroborated by the findings of [4] and [5]. The constant ratio of time steps with mesh element size was ($\frac{\Delta t}{\Delta x} = 1 \times 10^{-3}$, 1×10^{-4} and 1×10^{-5} s/m), determined based on the completed flow patterns along the perforated horizontal wellbore and also the convergence of the simulation.

Figure 7 showcases the variations in void fraction for various mesh sizes while simulating slug flow with a superficial velocity of 0.5 m/s for both air and water phases. Mesh size A (75,000 cells) exhibited an unclear slug flow pattern due to the influence of the interface separating bubbles. This effect was significantly less pronounced with mesh size B (1,000,000 cells), which displayed a distinct slug flow pattern with a quicker separation of radial airflow emanating from the top perforation. This phenomenon can be attributed to surface tension and shear stress.

The simulation period for mesh size B required approximately 7 days, corresponding to a simulation time of 7.2 s. In contrast, mesh size C (1,500,000 cells) yielded a void fraction of the air phase that resembled a stratified flow pattern, with a simulation period of 9 days and a simulation time of 8.9 s. Finally, mesh size D (2,000,000 cells) demonstrated a void fraction behavior indicative of a stratified flow pattern. The increased mesh size in this case exacerbated the impact of the interface, hindering the separation of air near the pipe wall. The simulation period for mesh size D was 13 days, corresponding to a simulation time of 11.4 s.

Figure 8 shows the static pressure drop distribution along the perforated horizontal pipe with different mesh sizes. A decrease in static pressure values is observed with increasing density of the mesh size. In this study, mesh size B type with (1,000,000 cells) was chosen as optimal because the slug flow pattern shape was very clear and the average static pressure drop value calculated experimentally converged from mesh size (1,000,000 cells), with a percentage error of 6.5% while it was (10.6%, 16.5%, and 18.5%) that occurs with (75,000 cells, 1,500,000 cells and 2,000,000 cells), respectively as explained in Table 1.

Furthermore, the simulation time associated with mesh size B was deemed favorable considering the available laptop specifications and the time required for result analysis.

Table 1. Error percentage of comparison Static pressure drop calculated experimentally with different mesh cell sizes

Number of cells	Average of static pressure drop (pa) numerical	Average of static pressure drop (pa) numerical	Error %
75000 cells	76.90	83.80	8.23 %
1,000,000 cells	80.40	83.80	4.29 %
1,500,000 cells	71.80	83.80	14.31 %
2,000,000 cells	70.04	83.80	16.42 %

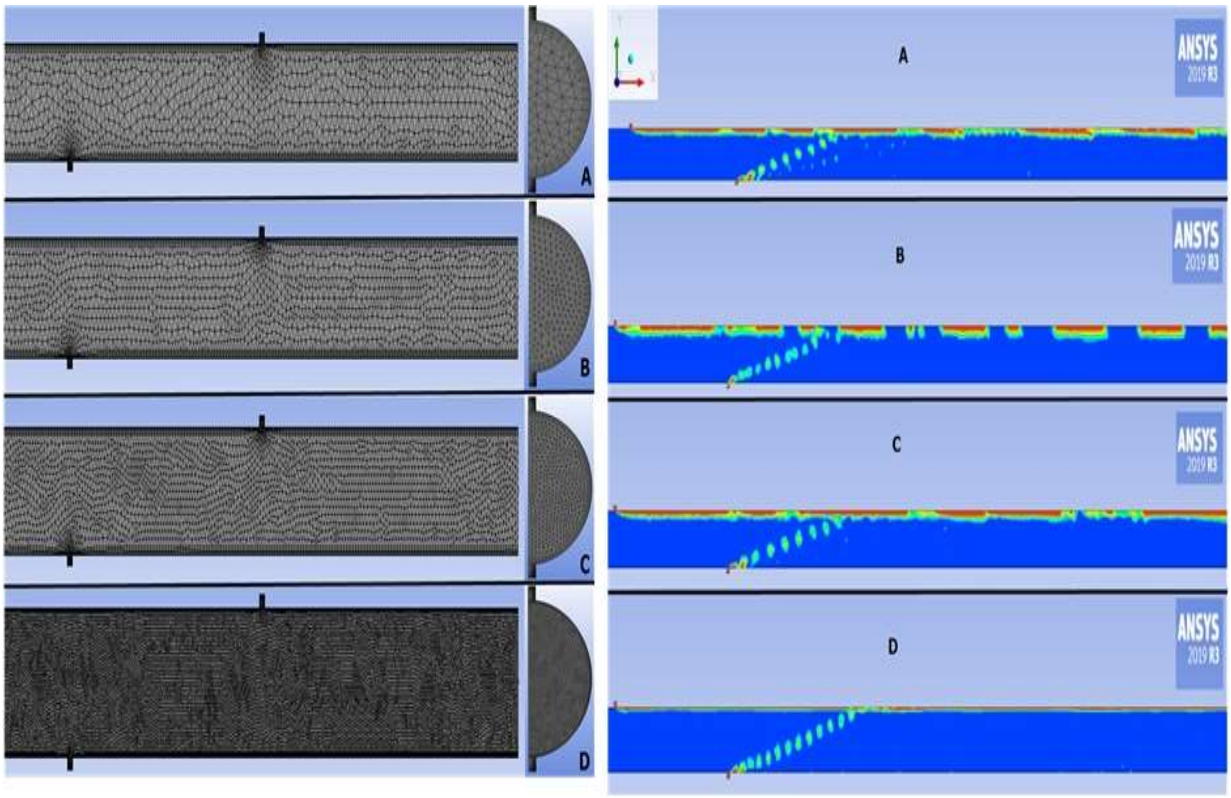

Fig. 7: Grid Independence of the plane when the x-axial (water phase) and the y-radial (air phase)

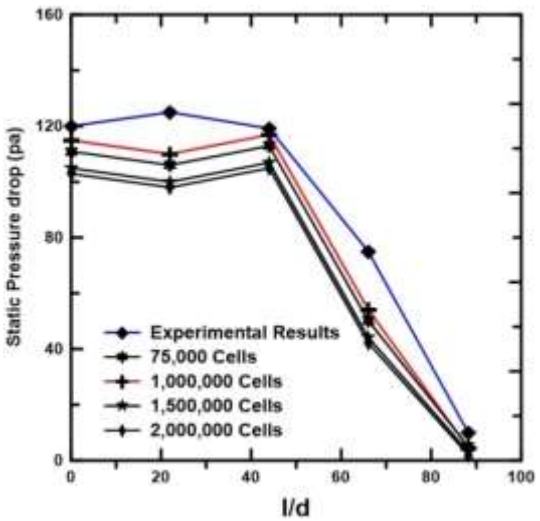

Fig. 8: Static pressure drop distribution along the pipe with different mesh sizes

3.3 Boundary Condition

The inlet boundary for two-phase flow is estimated using the following equation proposed by [24].

The superficial velocity of air: $U_{as} = \frac{Q_a}{A_m}$ (1)

The superficial velocity of water: $U_{ws} = \frac{Q_w}{A_m}$ (2)

Where: $A_m = A_a + A_w$ (3)

The inlet values for turbulent kinetic energy k, and its dissipation rate ε, are estimated using the following equation by [25].

$$k_{im} = \frac{3}{2} I^2 U_{\text{in}}^2 , \ \varepsilon_{in} = s k_{in}^{3/2} / D , \ I = \frac{0.16}{\text{Re}^{1/8}} \quad (4)$$

Where: *I* is turbulence intensity for fully developed pipe flow.

The outlet boundary is static pressure equal to zero because the perforated pipe's end is open and exhibits atmospheric pressure.

$$p = p^{\circ} = 0 \tag{5}$$

$$\frac{dU_m}{dx} = \frac{dV_m}{dy} = \frac{dW_m}{dz} = 0 \tag{6}$$

The mixture of two-phase flow is assumed to be a no-slip boundary condition on the wall of the pipe, defined as:

$$U_m = V_m = W_m = 0 \tag{7}$$

3.4 Governing Equations

The governing flow equations explain the solution of the two-phase (air-water) flow through the domain by balancing the mass and momentum equations as a function of the volume fraction values for each phase.

3.4.1 Conservation of Mass

The continuity equation is solved by the volume fraction of one or more of the phases. This equation has the following form for the q^{th} Liquid volume fraction phase, [24], [25].

$$\frac{1}{\rho_q}\left[\frac{d}{dt}\left(\alpha_q \rho_q\right) + \nabla.\left(\alpha_q \rho_q \vec{V_q}\right) = S_{\alpha_q} + \sum_{P=1}^{n}\left(\dot{m}_{pq} - \dot{m}_{qp}\right)\right] \tag{8}$$

$$\text{Where: } \vec{V} = U_i + V_j + W_k \tag{9}$$

$\dot{m}_{pq}$ explains the mass transfer from P to q and $\dot{m}_{qp}$ is the mass transfer from q to P, S_{α_q}: Source term.

The general continuity equation for mixture flow is given by [26].

$$\frac{d\rho_m}{dt} + \frac{d}{dx_i}\left(\rho U_m\right) = 0 \tag{10}$$

3.4.2 Conservation of Momentum

The momentum equation is solved in the full range as a function of the volume fractions of all phases, illustrated by vectors through the properties and defined as.

$$\frac{d}{dt}\left(\rho \vec{V}\right) + \nabla.\left(\rho \vec{V}\,\vec{V}\right) = -\nabla P + \rho \vec{g} + \nabla.\left[\mu\left(\nabla \vec{V} + \nabla \vec{V}^{T}\right)\right] + \vec{F} \tag{11}$$

The general momentum equation for mixture flow is defined as.

$$\frac{d(\rho_m U_j)}{dt} + \frac{d}{dx_j}\left(\rho_m U_i U_j\right) = -\frac{dp}{dx_i} + \rho_m g_j + \frac{d}{dx_j}\left[\mu_m\left(\frac{dU_i}{dx_j} + \frac{dU_j}{dx_i}\right) - \rho_m \overline{u_i' u_j'}\right] + \vec{F} \tag{12}$$

The error percentage is calculated using the mean absolute percent error (MAPE) that finds simply the average values of each column, as given by [27].

$$MAPE = \frac{1}{n}\sum \frac{|f_{pre} - f_{exp}|}{f_{exp}}\ 100\% \tag{13}$$

3.5 The Analysis of the Flow Patterns in a Perforated Horizontal Pipe (Numerical Study)

Figure 9 and Figure 10 illustrate the diverse flow regimes observed within a perforated horizontal pipe under various superficial air and water velocities. In Figure 9, the water superficial velocity is held constant at 0.27 m/s, while the air superficial velocity is incrementally increased. Case 1.1 depicts the bubble flow regime, where the dispersed air phase coexists with the continuous water phase. This regime arises due to the dominance of buoyancy and the contrasting physical properties (viscosity and density) of the air and water phases. The shear stress and surface tension of the water phase, coupled with the density difference, facilitate the formation of bubbles that accumulate at the pipe's upper section. These bubbles exhibit varying sizes and shapes but tend towards sphericity.

As evident in Case 1.2, increasing the air's superficial velocity leads to the coalescence of individual bubbles into larger entities. Further augmentation of the airflow rate, as shown in Case 1.3, results in the formation of slug flow, characterized by elongated air pockets separated by water layers. The buoyancy force and varying mixture concentrations (air and water) contribute to the segregation of these air gaps within the pipe. These distinct air pockets resemble large waves that can potentially fill the entire pipe diameter. Case 1.4 demonstrates the further enlargement and merging of air gaps into Taylor bubbles with increasing air superficial velocity. Finally, Case 1.5 showcases the

stratified flow regime observed at a superficial air velocity of 1.7 m/s. Buoyancy compels the air phase to accumulate at the pipe's top, while gravity governs the downward flow of the water phase. Notably, a critical air superficial velocity of 2.6 m/s (Case 1.6) is observed beyond which the radial air flow overcomes the axial water flow, leading to an undesirable reverse flow. This phenomenon signifies a detrimental loss in oil production, highlighting the importance of maintaining airflow rates within acceptable limits. It is also noteworthy that stratified flow is consistently observed at the end of the pipe across all patterns, owing to the insufficiency of axial water flow to completely fill the pipe.

Figure 10 presents flow regimes obtained with a higher water superficial velocity of 0.55 m/s, exhibiting similar trends to those observed in Figure 7. Notably, Cases 2.7, 2.8, and 2.9 depict the occurrence of stratified wave flow due to the high air superficial velocity, which possesses sufficient kinetic energy to entrain the water phase and generate waves within the perforated pipe. Case 2.7 exemplifies the coexistence of stratified flow at the upper perforations and bubble flow at the lower perforations, attributed to the interplay of shear stress, surface tension, and water phase concentration. As the air superficial velocity increases in Case 2.8, the flow regime transitions from stratified to stratified wave flow, reflecting the generation of numerous waves within the pipe due to the high kinetic energy of the air phase. Case 2.9 showcases the transition from stratified wave to annular flow at an air superficial velocity of 33.1 m/s.

The high air velocity propels the air phase towards the pipe's center, forcing the water phase towards the wall. While annular flow is prevalent near the perforations, it transitions back to stratified wave flow at a distance of 2-3 meters from the mean inlet due to the influence of gravity on the water phase. Furthermore, the insufficient kinetic energy of the airflow in this case study (mentioned in Table 2) leads to the formation of stratified wave flow in the central region of the perforated horizontal pipe.

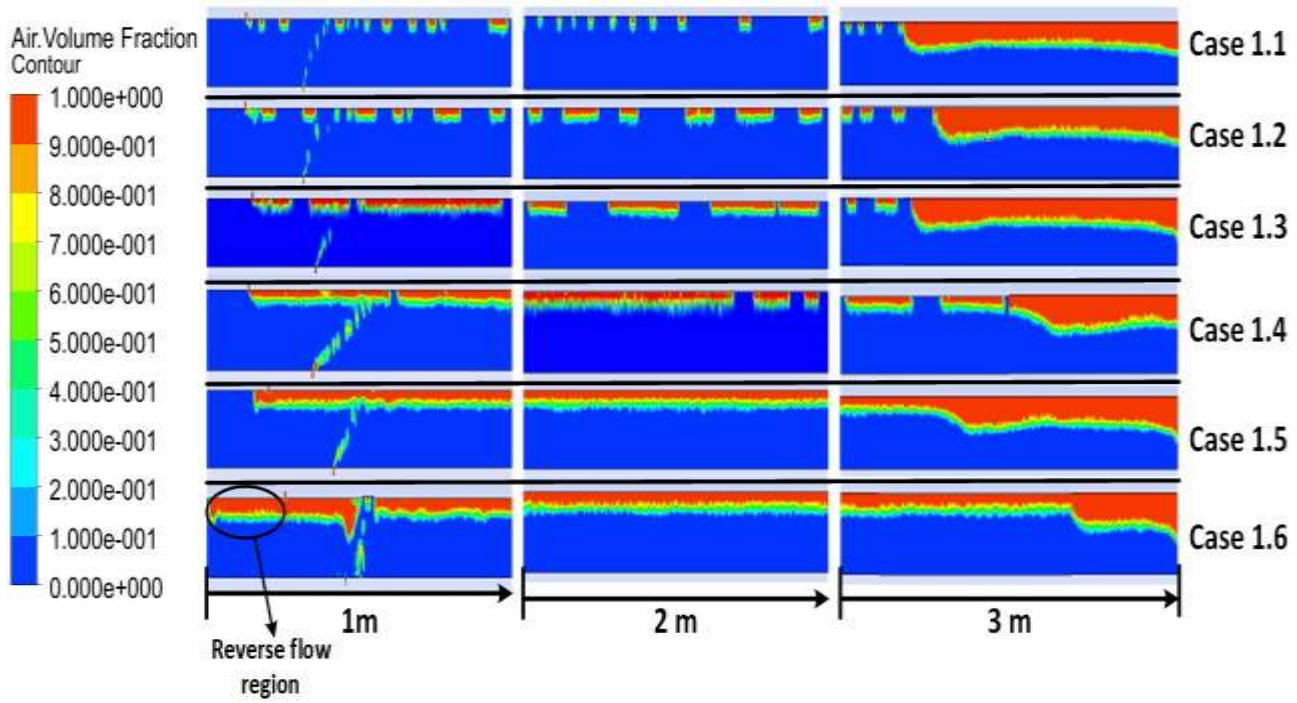

Fig. 9: Flow patterns in the perforated horizontal pipe when U_{ws} = 0.27 m/s

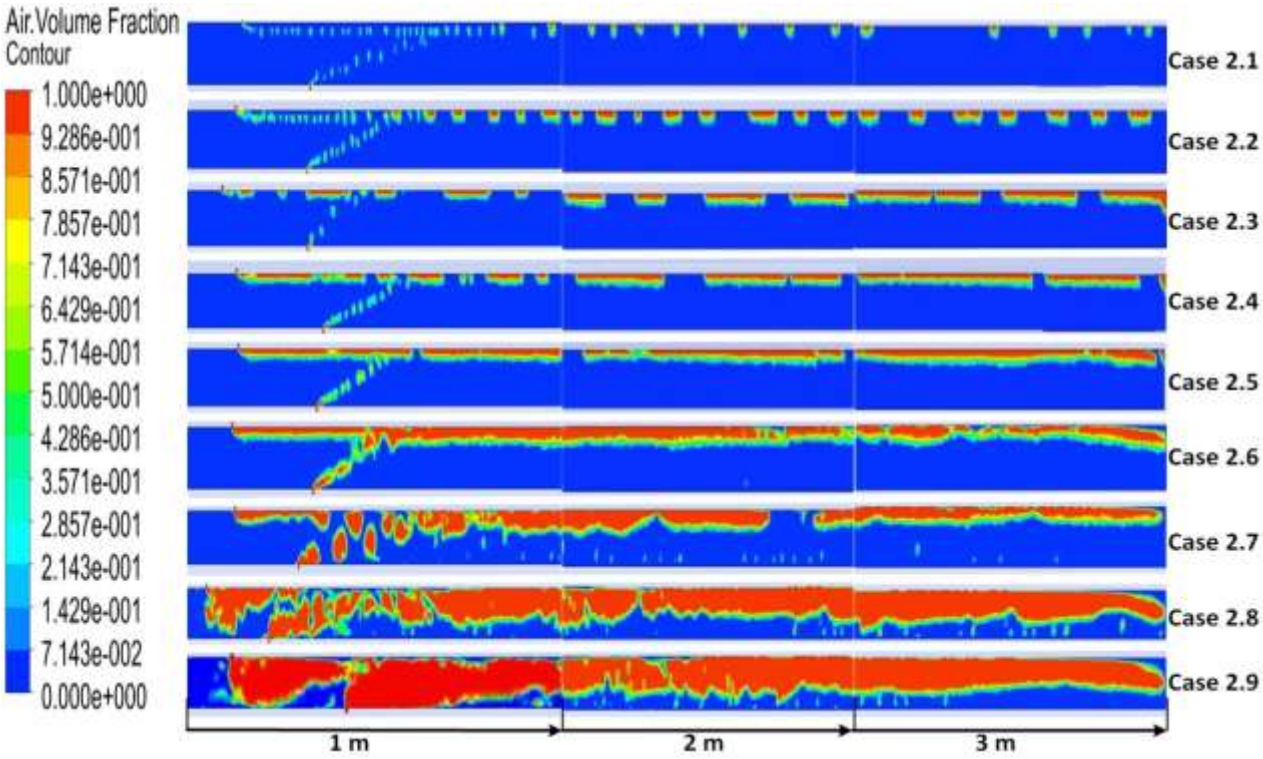

Fig. 10: Flow patterns in the perforated horizontal pipe when U_{ws} = 0.55 m/s

Table 2. A case study of flow patterns

Test No.	Flow patterns	U_{as} m/s	U_{ws} m/s	Test No	Flow patterns	U_{as} m/s	U_{ws} m/s
Case 1.1	Bubble flow	0.066	0.27	Case 2.1	Bubble flow	0.066	0.55
Case 1.2	Transition bubble/slug flow	0.1	0.27	Case 2.2	Transition bubble/dispersed flow	0.1	0.55
Case 1.3	Slug flow	0.3	0.27	Case 2.3	Slug flow	0.3	0.55
Case 1.4	Taylor bubble	0.5	0.27	Case 2.4	Transition Slug/Taylor	0.5	0.55
Case 1.5	Stratified flow	1.3	0.27	Case 2.5	Taylor bubble	1.3	0.55
Case 1.6	Stratified flow	2.6	0.27	Case 2.6	Stratified flow	6.6	0.55
				Case 2.7	Transition slug/ stratified wave flow	10.5	0.55
				Case 2.8	Stratified wave flow	19.8	0.55
				Case 2.9	Transition stratified wave/ annular flow	33.1	0.55

4 Result and Discussion

4.1 The Behavior of Static Pressure Drop with the Bubble Flow Pattern

Figure 11 presents the behavior of static pressure drop (Pa) over time (s) during the bubble flow pattern in the perforated horizontal pipe (Case 1). At the inlet region, the pressure drop values remain constant due to the dominance of the water phase.

As the flow progresses towards the perforations (sensor pressure l/d = 22 and 44), the increasing mixing pressure drop in this region, caused by the disparity in density between the air and water phases, leads to increased pressure fluctuations.

The pressure drop exhibits a cyclical pattern, increasing as the water phase passes through the sensor's cross-sectional area and decreasing as the bubble phase passes through. This trend continues

along the horizontal pipe, with the pressure drop decreasing from inlet to outlet due to frictional losses. The variation in pressure drop magnitude is influenced by the size and kinetic energy of the bubbles, with a higher concentration observed at sensor pressure l/d = 66 due to its location in a fully developed flow region.

Moreover, void friction increases with the length of the perforated horizontal pipe. Finally, the pressure sensor values in the outlet region remain stable due to the low static pressure drop readings, resulting in minimal oscillations.

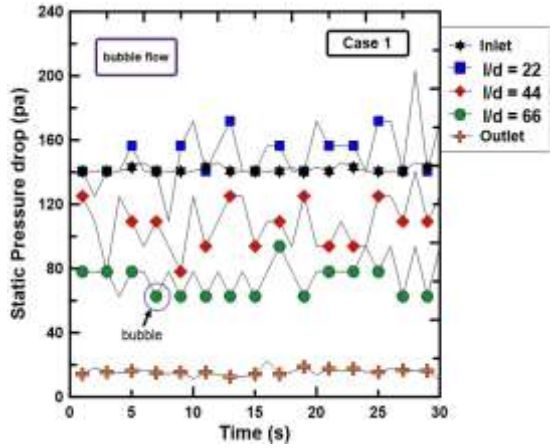

Fig. 11: Bubble flow when the superficial air velocity is 0.066 m/s, and the superficial water velocity is 0.27 m/s

Figure 12 shows Case 2, which demonstrates a reduction in fluctuation during the bubble flow pattern with increased water superficial velocity. Static pressure drop values increase with increasing water superficial velocity due to the impact of water phase concentration and density. Fluctuation during this flow pattern is lower compared to Case 1 as bubble size is smaller when superficial water velocity is 0.55 m/s.

A decrease in bubble count is observed with increasing water superficial velocity, resulting in increased holdup fraction values and greater distance between generated bubbles. Pressure sensor values are more stable during this regime.

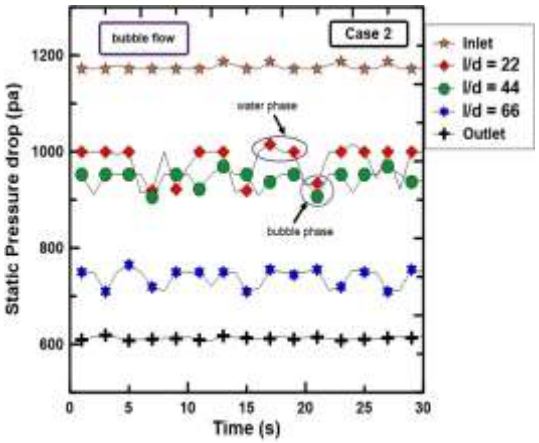

Fig. 12: Bubble flow when superficial air velocity is 0.066 m/s and superficial water velocity is 0.55 m/s

4.2 The Behavior of Static Pressure Drop with Transition Bubble/ Slug Flow Pattern

As shown in Figure 13 (Case 3), increasing the air superficial velocity leads to the formation of a large air gap separated by a water layer, known as the transition bubble/slug flow pattern. This phenomenon primarily occurs in the fully developed region, where the mixture flow velocity reaches its maximum value. Consequently, the static pressure drop remains stable throughout the slug phase due to minimal air phase fluctuations. In this scenario, the pressure sensor effectively treats the air phase as a single phase due to its reduced sensitivity to individual bubbles.

Notably, the size of the bubbles influences the static pressure drop, with larger bubbles resulting in a higher pressure drop. The occurrence of this flow pattern is dependent on the air's superficial velocity, with faster velocities causing it to appear earlier.

4.3 The Behavior of Static Pressure Drop with Transition Bubble/ Dispersed Bubble Flow Pattern

Figure 14 (Case 4) illustrates the transition bubble/dispersed bubble flow pattern resulting from an increase in water superficial velocity while maintaining a constant air superficial velocity. The presence of more bubbles at the pressure sensor location (l/d = 66) leads to increased fluctuations due to the higher bubble count along the perforated horizontal pipe.

In this flow pattern, individual bubbles have equal kinetic energy, preventing them from merging and forming larger bubbles. As a result, the pressure sensor readings stay consistent with those observed in Case 1.

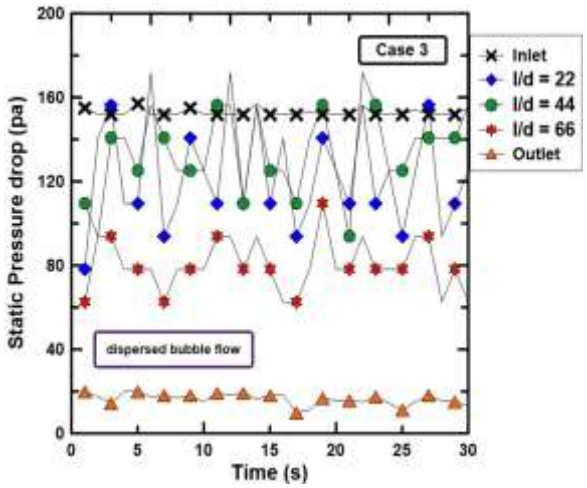

Fig. 13: Transition bubble/slug flow when the superficial air velocity is 0.1 m/s, and the superficial water velocity is 0.27 m/s

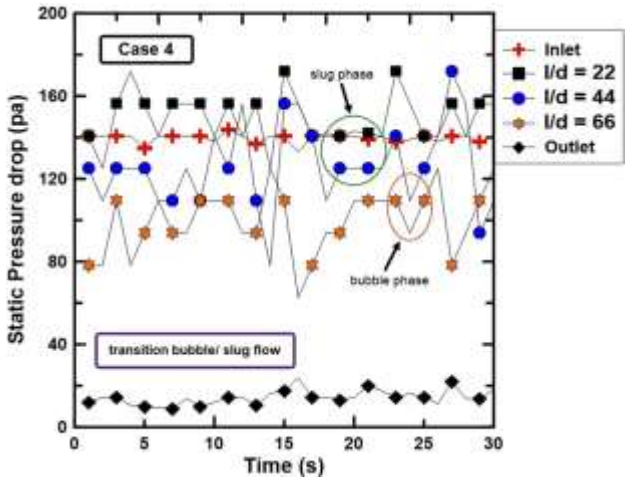

Fig. 14: Transition bubble/dispersed flow when the superficial air velocity is 0.1 m/s, and the superficial water velocity is 0.55 m/s

4.4 The Behavior of Static Pressure Drop with the Slug Flow Pattern

Figure 15 outlines Case 5, which examines the behavior of static pressure drop during the slug flow pattern. The static pressure drop values decrease during the period from 5 to 10 seconds, indicating a slug situation influenced by the air phase. Conversely, an increase in static pressure drop from 10 to 15 seconds signifies the passage of the water phase through a cross-sectional measurement region of the pressure sensor. The oscillation of static pressure drop value is attributed to differences in density and viscosity between air and water phases. The outlet pressure sensor also reflects the influence of slug flow, with values and fluctuation of static pressure drop decreasing as water superficial velocity increases and holdup fraction rises.

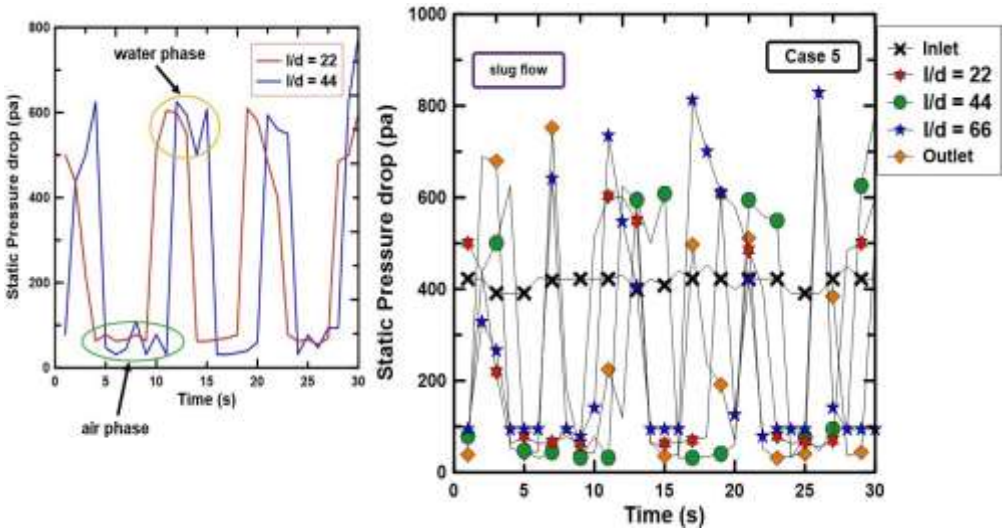

Fig. 15: Slug flow when superficial air velocity is 0.3 m/s

4.5 The Behavior of Static Pressure Drop with the Stratified Flow Pattern

Figure 16 (Case 6) depicts the stratified flow pattern, where the air phase accumulates at the top of the horizontal pipe due to the buoyant force acting on the lighter air. Conversely, the water phase settles at the bottom of the pipe due to the gravitational force acting on the denser water. In this flow pattern, the pressure sensor is primarily sensitive to the air phase; consequently, the static pressure drop values exhibit greater stability. However, some fluctuations are observed in the pressure sensor readings at l/d = 22 and l/d = 44, as these locations are close to the perforations where the mixing pressure drop, arising from the interaction between radial and axial flow phases, exerts an influence.

Additionally, the superficial velocity of the mixture flow demonstrates instability within this range. Beyond this region, at l/d = 66, the static pressure drop values become more stable as the mixture flow reaches the fully developed region and moves further away from the influence of the perforations.

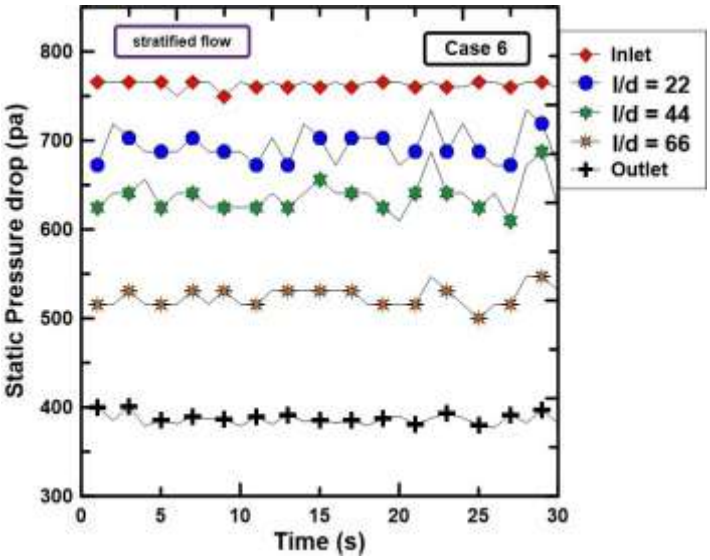

Fig. 16: Stratified flow when superficial air velocity is 1.3 m/s

4.6 The Behavior of Static Pressure Drop with Transition Slug/ Stratified Wave Flow Pattern

Figure 17 (Case 7) depicts the transition from slug flow to a stratified wave flow pattern as the air superficial velocity increases. This transition is accompanied by a rise in void fraction compared to Case 5. The high kinetic energy of the air phase leads to the formation of waves within the pipe, while the increased void fraction and decreased holdup fraction result in a reduction of the water layer separating the air gaps.

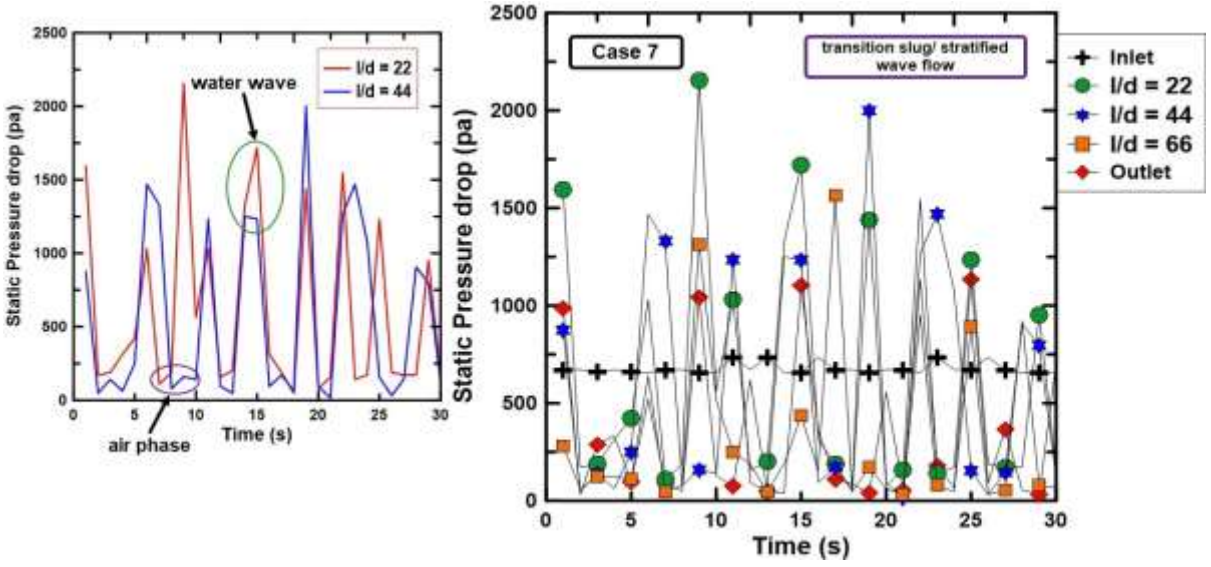

Fig. 17: Transition slug/ stratified wave flow when superficial air velocity is 10.5 m/s

4.7 The Behavior of Static Pressure Drop with the Stratified Wave Flow Pattern

Figure 18 showcases Case 8, illustrating the formation of a stratified wave flow pattern under constant superficial water velocity and high superficial air velocity. The substantial air velocity effectively entrains the water phase, leading to the generation of high-amplitude waves on the interface between the two phases. These waves play a critical role in the observed pressure drop behavior. The kinetic energy associated with the wave motion directly influences the static pressure drop, with higher kinetic energy corresponding to a greater pressure drop and vice versa.

In Figure 19, Case 9, it is evident that the stratified wave flow pattern is semi-stable. The waves formed in this case exhibit higher peaks compared to the previous Case 8, and this is contingent upon the kinetic energy when the superficial water velocity is 0.55 m/s. Additionally, when the superficial water velocity is increased, a slight fluctuation is observed, leading to the formation of waves at regular intervals. Consequently, the pressure drop increases due to the augmented mixture of superficial velocity.

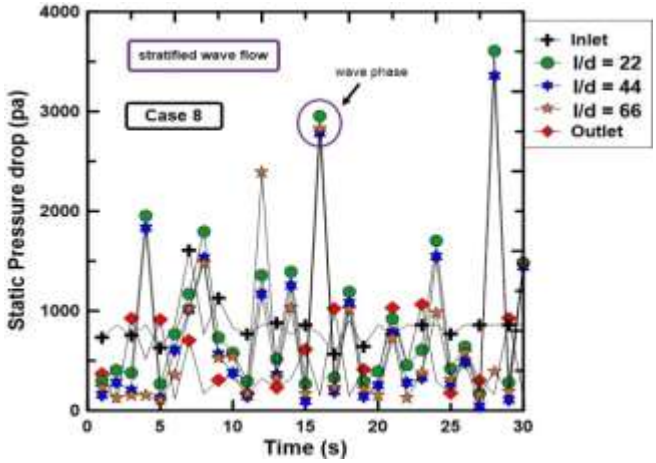

Fig. 18: Stratified wave flow when the superficial air velocity is 19.8 m/s

4.8 The Behavior of Static Pressure Drop of Flow Patterns with l/d

4.8.1 Influence of l/d Ratio on Static Pressure Drop

Figure 20 illustrates the impact of l/d on static pressure drop (Pa) across various flow patterns while maintaining a constant water superficial velocity and varying air superficial velocity. The results demonstrate fluctuations in static pressure drop when l/d ranges from approximately 20 to 60. Beyond this range, a continuous reduction is observed towards a stable state indicative of fully developed flow. This region signifies the achievement of a steady-state regime with a well-defined mixture flow profile. Notably, a peak in pressure drop occurs at l/d = 22, attributed to the reduction in axial flow hindering radial flow and consequently increasing the mixing pressure drop. This phenomenon is particularly evident during bubble, dispersed bubble, and slug flow regimes.

In contrast, stratified flow exhibits a stable decline in static pressure drop along the perforated horizontal pipe as l/d increases. This behavior arises from the air and water phases approaching equal superficial velocities, resulting in the pressure sensor being primarily influenced by the air phase. This flow pattern manifests due to the air phase accumulating at the upper portion of the horizontal pipe, while the water phase accumulates at the bottom.

During stratified wave flow, the observed oscillations in static pressure drop are directly linked to the kinetic energy of the generated waves. Higher kinetic energy translates to increased static pressure drop.

4.8.2 Impact of Water Superficial Velocity

Figure 21 depicts the influence of increasing water superficial velocity on the behavior of static pressure drop. Notably, the trend becomes smoother with less pronounced fluctuations, likely due to the presence of a higher holdup fraction. This observation aligns with the decreasing trend in static pressure drop values as the flow regime transitions from bubble to stratified with increasing air superficial velocity. Bubble flow exhibits the highest static pressure drop, followed by a decrease in the stratified flow regime. This disparity can be attributed to the pressure sensor in the stratified flow pattern solely experiencing the influence of the air phase. Furthermore, the transition between flow regimes is governed by the increasing air superficial velocity.

Lastly, the static pressure drop associated with stratified wave flow surpasses that of slug and stratified flow patterns. This phenomenon is attributed to the number and size of generated waves. A greater number and size of waves contribute to a higher static pressure drop, as the kinetic energy of the mixture flow during this pattern is significantly higher compared to other regimes.

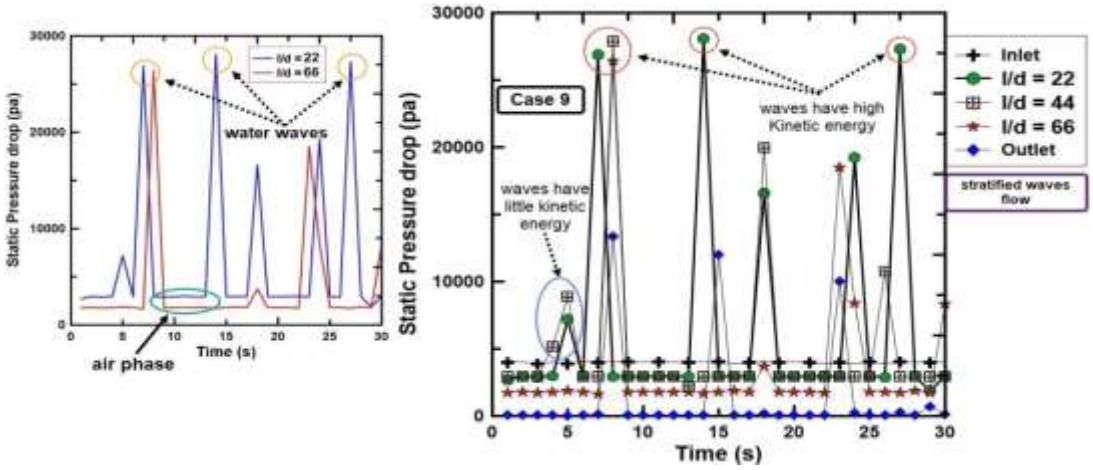

Fig. 19: Stratified wave flow when the superficial air velocity is 33.1 m/s

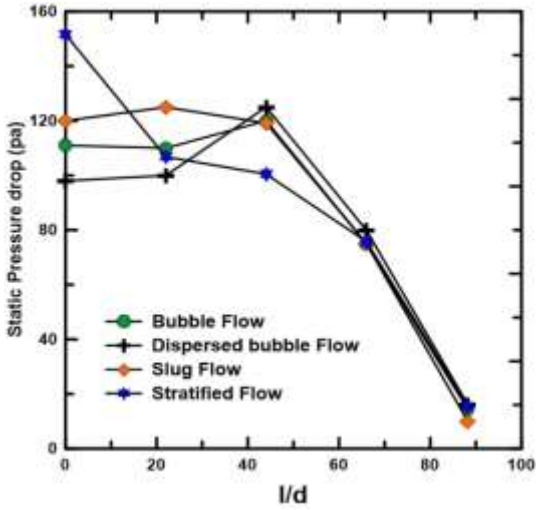

Fig. 20: The behavior of static pressure drop when superficial water velocity is 0.27 m/s

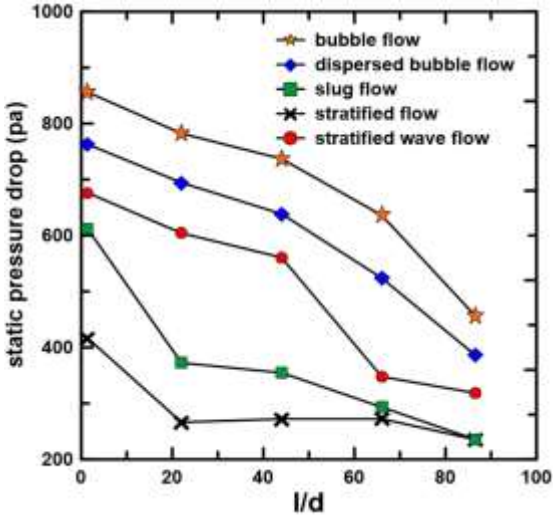

Fig. 21: The behavior of static pressure drop when superficial water velocity is 0.55 m/s.

4.9 Impact of Friction Factor through the Unperforated and Perforated Horizontal Pipes

Figure 22 illustrates the relationship between the friction factor through perforated and unperforated horizontal pipes and the Reynolds number of mixture flow (Re_m). A decrease in friction factor is observed with an increased Reynolds number of mixture flow, in accordance with Equations (8) and (9). Perforation roughness, as described by Equation (9), is dependent on universal velocity, density of perforations, and perforation diameter relative to a perforated horizontal pipe.

The friction factor value is 0.031 when the Reynolds number is 9162, decreasing to 0.025 when the Reynolds number is 21380, as determined by the Haaland Equation (Equation 8). Using Equation (9), the friction factor is calculated as 0.03146 at a Reynolds number of 9162 and decreases to 0.02512 at a Reynolds number of 21380. The resulting error percentage is 1.4% at a Reynolds number of 9162 and 0.48% at a Reynolds number of 21380.

Therefore, it can be concluded that the comparison of friction factor values (perforated and unperforated horizontal pipe) approaches each other with increasing Reynolds numbers due to the reduced impact of friction at higher Reynolds numbers and vice versa.

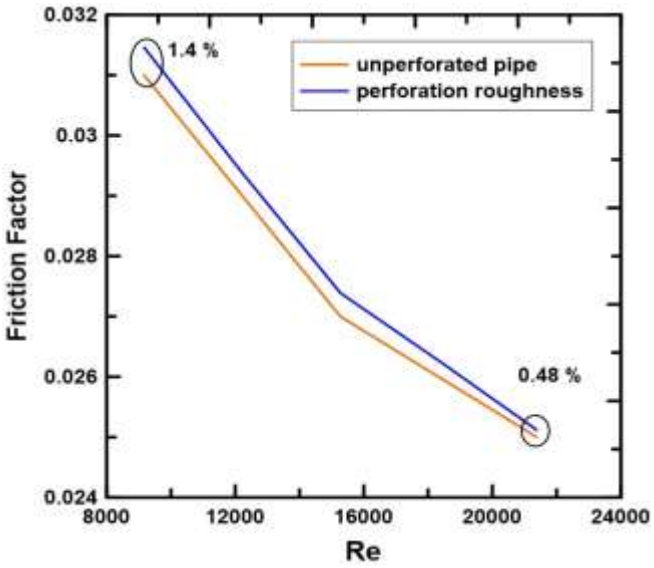

Fig. 22: Friction factors with the unperforated and perforated horizontal pipes

4.10 Comparison between Experimental and Numerical Results

Figure 23 presents a comparison between the experimental and numerical results for the static pressure drop along the pipe. The behavior of the pressure drop curve exhibits a distinct increase at the point l/d = 44 (length-to-diameter ratio). This can be attributed to the combined effects of the flow pattern (bubble, dispersed bubble, and slug flow) at this location and the presence of the perforated section. Additionally, the interaction between the air and water phases (two-phase flow) contributes to the pressure rise at this point. Furthermore, the mixing and frictional pressure drops are also intensified due to the flow characteristics.

The introduction of stratified wave flow further contributes to the pressure increase at l/d = 44. This phenomenon is associated with the high air flow rate (while maintaining a constant water flow rate) and the wave formation characteristic of this flow pattern. The unsteady nature of the flow, corresponding to a two-phase flow not yet reaching a stable state, further amplifies the pressure drop behavior. Conversely, for slug and stratified flows (occurring at air-to-water flow rate ratios near unity), the pressure drop curve becomes more streamlined and stable. This is because these flow patterns represent a closer approximation to single-phase flow, leading to a steady state along the pipe.

4.10.1 Steady-State Flow Characteristics

Under steady-state conditions, the flow regime exhibits a clear stratification, with the air phase occupying the upper portion of the pipe due to buoyancy, while the water phase flows downwards driven by gravity. Since the static pressure drop is measured at the upper surface, it is primarily influenced by the air phase (acting as a single phase) due to its significantly lower density and viscosity compared to water. Additionally, the compressible nature of air and the minimal frictional effect further contribute to its negligible impact on the pressure drop.

4.10.2 Flow Pattern Dependence and Convergence

The analysis reveals a general trend of decreasing static pressure drop along the horizontal pipe with increasing air flow rate (while maintaining a constant water flow rate), reflecting the transition between different flow patterns. Notably, the pressure drop converges to a small value (close to atmospheric pressure) at the outlet region (l/d = 88) for all flow patterns. This implies that the pressure drop difference at the outlet is negligible.

Figure 24 visually demonstrates the comparison between experimental and numerical results by presenting the air fraction contours extracted numerically along the perforated wellbore. This visualization underscores the clear relationship between the flow patterns observed in the fully developed region.

4.10.3 Error Analysis

Table 3 summarizes the calculated error percentages (using Equation 6) for the different flow patterns. An increased error percentage (12.49%) is observed for stratified wave flow due to the elevated air flow rate inducing water wave formation. These waves contribute to increased fluctuations in both experimental and numerical data, leading to a higher error percentage. Conversely, flow patterns exhibiting behavior closer to single-phase flow (streamline), namely slug and stratified flows, demonstrate lower error percentages (3.67% and 1.53%, respectively).

Figure 25 complements the analysis by illustrating the occurrence of the reverse flow region when the radial air flow rate surpasses the axial water flow rate, as detailed in Figure 9 (Case 1.6).

Table 3. Percentage Error of Flow Patterns Comparison

Air Flow rate (l/m)	Water Flow rate (l/m)	Average of experimental results	Average of numerical results	Flow Patterns	٪Error
0.05	15	86.08	77.25	Bubble Flow	10.25 %
0.1	15	89.83	80.10	Dispersed Bubble Flow	10.83 %
0.5	15	83.80	80.72	Slug Flow	3.67 %
5	15	90.04	91.42	Stratified Flow	1.53 %
15	15	475.38	416.2	Stratified Wave Flow	12.49 %

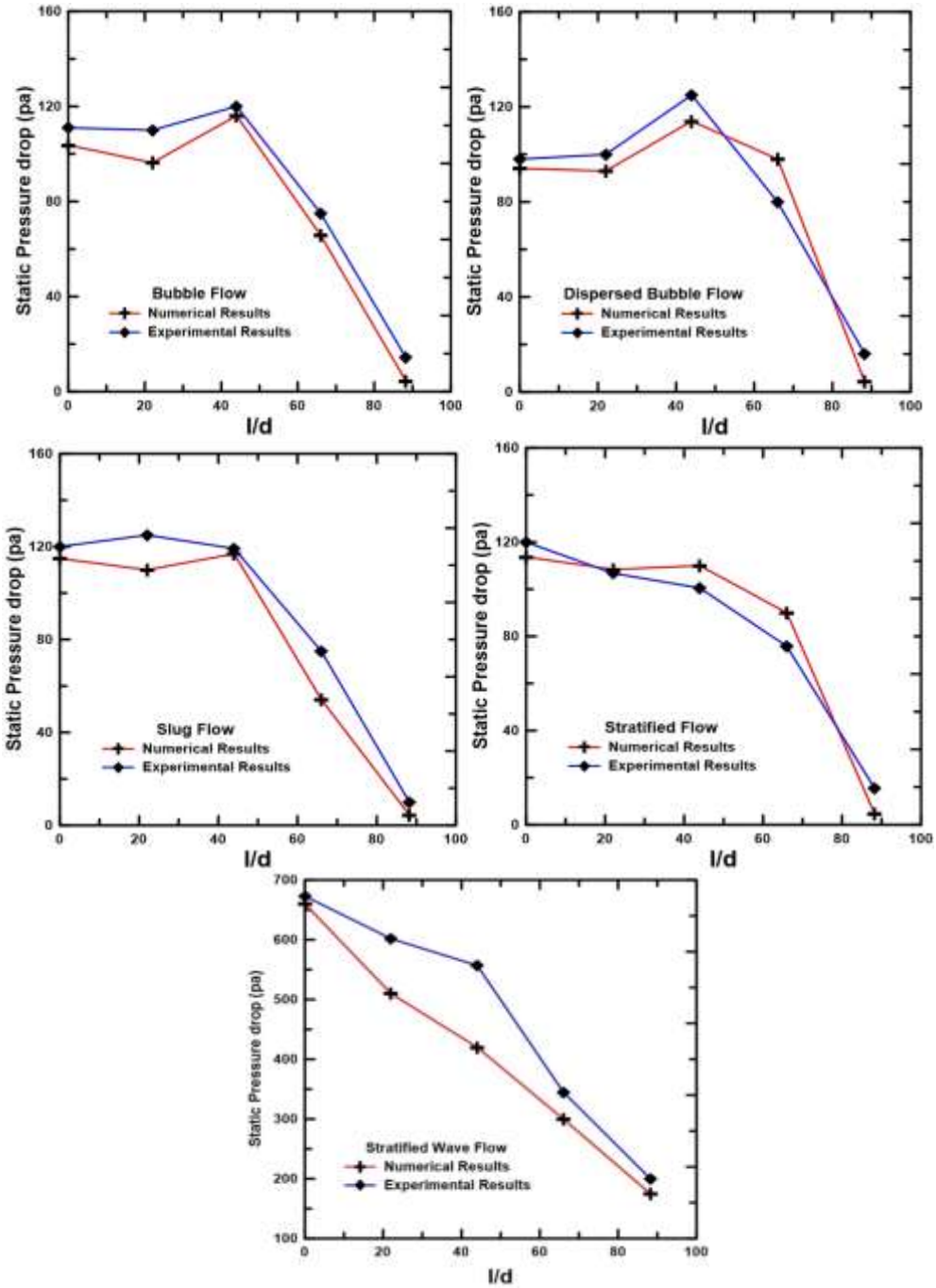

Fig. 23: The comparison of static pressure drop between experimental and numerical results

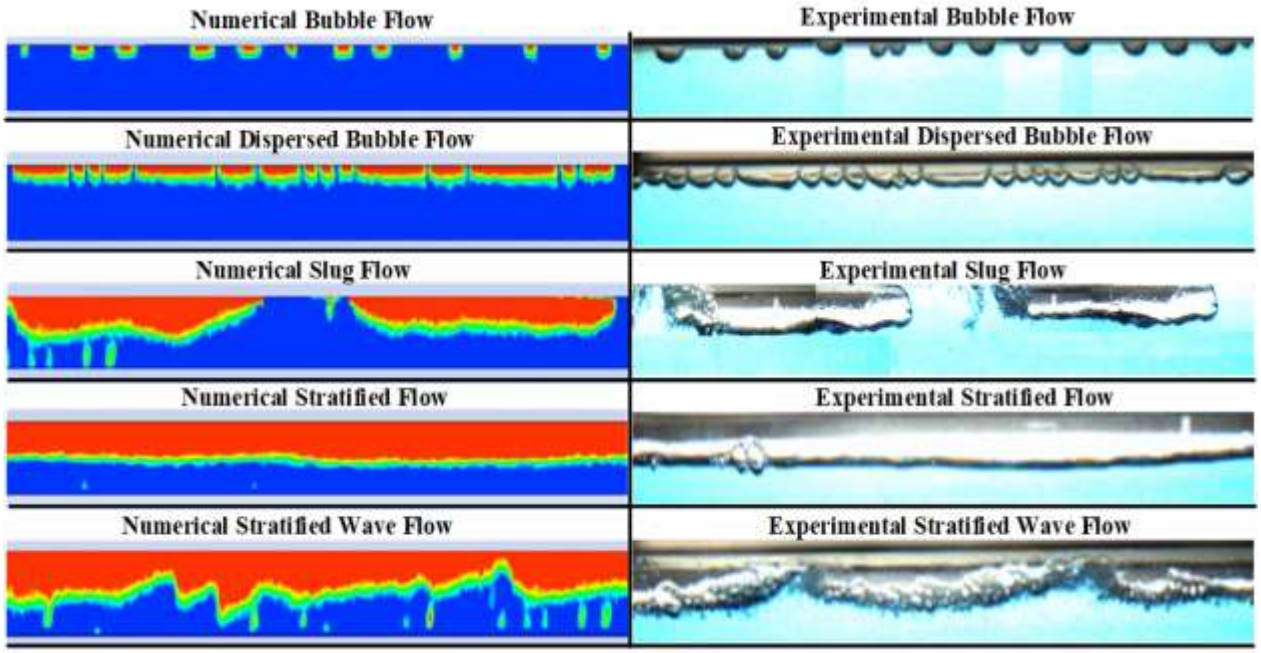

Fig. 24: The comparison of flow patterns between experimental and numerical results

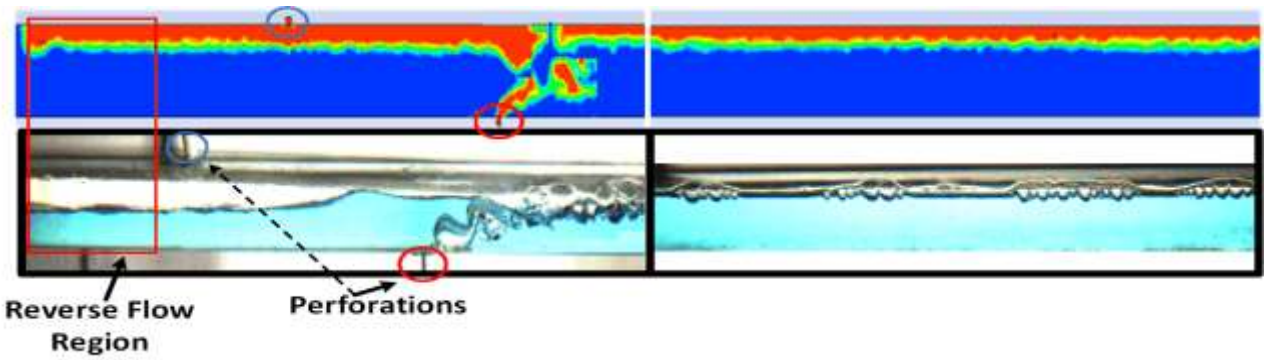

Fig. 25: Reverse flow region

4.11 Measuring Liquid Product Quantity in Horizontal Wells

This study explores a method for measuring the quantity of liquid product extracted from a horizontal wellbore during a production process. The extracted liquid, typically a multiphase mixture of oil, water, and gas, requires separation at petroleum installations to obtain the final product, crude oil. The wellbore's productivity, ultimately determining its success, is directly correlated with the amount of oil produced. Traditionally, the productivity index, developed for single-phase flow, has been used to estimate productivity in some cases. However, this approach assumes that the liquid flowing out of a perforated horizontal pipe directly translates to the amount of oil produced, which is not entirely accurate in multiphase flow situations.

The proposed method for measuring the liquid product quantity utilizes a dedicated setup featuring two tanks: a 20-liter test tank for collecting the liquid product over a specified time and a holding tank for accumulating the returned liquid before reinjection into the storage tank (Figure 26). When the two-phase flow enters the test tank, the air components separate and are released upwards due to their lower density compared to the water, which settles at the bottom due to gravity.

To determine the liquid quantity, the weight (in kilograms) is measured using a scale and then divided by the fixed measurement time (two minutes) established using a stopwatch. Control valves 1 and 2 are employed to manage the opening and closing of the pipe after each reading. For measurement, valve 1 is closed, and valve 2 is opened, allowing the liquid in the test tank to be weighed.

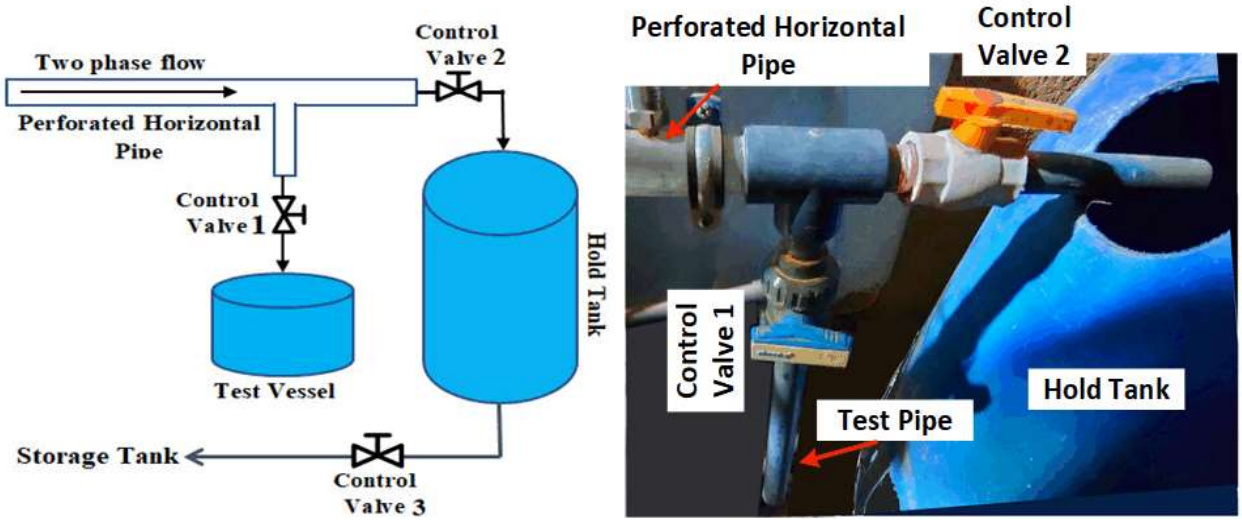

Fig. 26: Procedure to measure the quantity of the liquid product

Standard parameter measurements are conducted with valve 1 open, valve 2 closed, and valve 3 open, maintaining a closed system.

To minimize measurement errors, the process is repeated approximately six times for each reading, with the final liquid quantity value determined by averaging the collected measurements. Additionally, a three-minute waiting period is implemented between each measurement to ensure system stability and allow for potential pressure fluctuations to subside. This multi-step approach offers a standardized and reliable method for measuring the liquid product quantity in horizontal wells, facilitating accurate wellbore productivity assessments, and optimizing oil production processes.

Figure 27 A–E demonstrates an increase in the quantity of liquid product collected with increasing air superficial velocity when water superficial velocity is kept constant. In Figure 27 A, when U_{ws} = 0.27 m/s, the quantity of the liquid product begins to increase from a value of 0.17 kg/s. When U_{as} = 0.066 m/s, the amount increases until a value of U_{as} = 0.33 kg/s is reached. When U_{as} = 1.32 m/s, both bubble and slug flows are observed. The quantity of the liquid product gradually decreases (during the transition from slug to stratified flow) that occurs during U_{as} = 10 m/s. After this velocity, the quantity is almost stable (during the transition from stratified to stratified wave flow). The reason for obtaining constant values of the liquid product is that the increase in the amount of air will have a minimum impact on the quantity of water. At the same time, the effect of friction and the mixing pressure drop between air and water decreased.

Figure 27 B exhibits similar behavior to Figure 27 A, with an increased drop in liquid product observed at air superficial velocities greater than U_{as} = 10 m/s (stratified wave flow) because of the impact of the increased velocity of the air phase. With an increase in the water superficial velocity (U_{ws} = 0.45 m/s) as indicated in Figure 27 C, it is observed that the quantity of the liquid product increases up to 0.46 kg/s when (U_{as} = 0.066 m/s) occurs during the bubble flow. On the contrary, a sharp drop in the value of the liquid product is observed with an increase in the air's superficial velocity. This drop will continue till it reaches about U_{as} = 0.43 kg/s, then return to an increase. It occurred because of an increase in the void fraction value through a transition from the stratified flow to the stratified wave flow pattern that caused a loss in the liquid product.

Figure 27 D explains the value of the liquid product at U_{ws} = 0.55 m/s. It was observed that the value of the liquid product is U_{ws} = 0.55 kg/s when U_{as} = 0.066 m/s and 1.32 m/s, respectively (when the transition from bubble to slug flow occurs). However, the liquid product increases during the transition from slug to stratified flow. Otherwise, the drop in the liquid product occurs when the transition from stratified flow to stratified wave

flow occurs, and this drop gets the shape of the concavity in the curve of values of the liquid product. Then it is increased when the air's superficial velocity is greater than $U_{as} = 40$ m/s.

Figure 27 E depicts an increase in the liquid product value during bubble flow and the transition from bubble to slug flow, reaching approximately 0.69 kg/s. However, a simultaneous drop in the liquid product value occurs during the transition from slug to stratified wave flow. This drop indicates fluctuations in the liquid product value due to its dependency on the generated waves. These waves lead to instability in the values and help increase the quantity of the liquid product.

Figure 28 illustrates a direct correlation between the average liquid product and the mixture's superficial velocity. This is attributed to the combined effect of an increasing holdup fraction, due to a higher water phase presence, and a larger volume flow rate associated with higher velocities. Table 4 presents details on the liquid product behavior observed during increased water superficial velocity.

Several Key Observations:

1. **Positive Correlation**: The quantity of liquid product exhibits a positive correlation with increasing water superficial velocity, primarily due to the rising holdup fraction.
2. **Flow Regime Dependence:** For bubble and slug flow regimes (air superficial velocity between 0.066 m/s and 1.32 m/s), the liquid product increases with rising water superficial velocity.
3. **Flow Regime Transition:** A decrease in the liquid product is observed during the transition from slug flow and stratified flow to stratified wave flow.
4. **Water Velocity Impact:** A sharper decline in the liquid product is observed at high water superficial velocities compared to lower ones.
5. **Stratified Wave Flow:** In some instances, stratified wave flow can exhibit an increase in the liquid product due to wave generation, leading to a higher holdup fraction and friction factor. However, increasing the air phase can counteract this effect by increasing the void fraction and decreasing the holdup fraction, resulting in a significant drop in the liquid product.
6. **Mixing Pressure Drop:** An increase in mixing pressure drop near perforation regions contributes to a further decrease in the liquid product. This phenomenon arises due to the hindering effect of air radial velocity on water axial velocity, creating a bottleneck region that restricts water flow and consequently, reduces the liquid product (particularly evident in stratified and stratified wave flows).
7. **Stratified Flow:** The stratified flow regime, characterized by two distinct phases with air accumulating at the top and water settling at the bottom due to buoyancy and gravity, respectively, exhibits a decrease in the liquid product. This is because high air superficial velocity has minimal influence on the water phase, except at the interface between the two phases. Notably, some stratified wave flow data points show higher liquid product values compared to stratified flow due to the influence of generated waves.
8. **Constant Air Velocity:** When air superficial velocity is maintained constant, the percentage of liquid product increases proportionally with increasing water superficial velocity.

Table 4. Data of average liquid product with water superficial velocity

No	Water Superficial Velocity m/s	Average of liquid product kg/s
1	0.27	0.561917
2	0.36	0.71945
3	0.45	0.91445
4	0.55	1.07135
5	0.63	1.298933

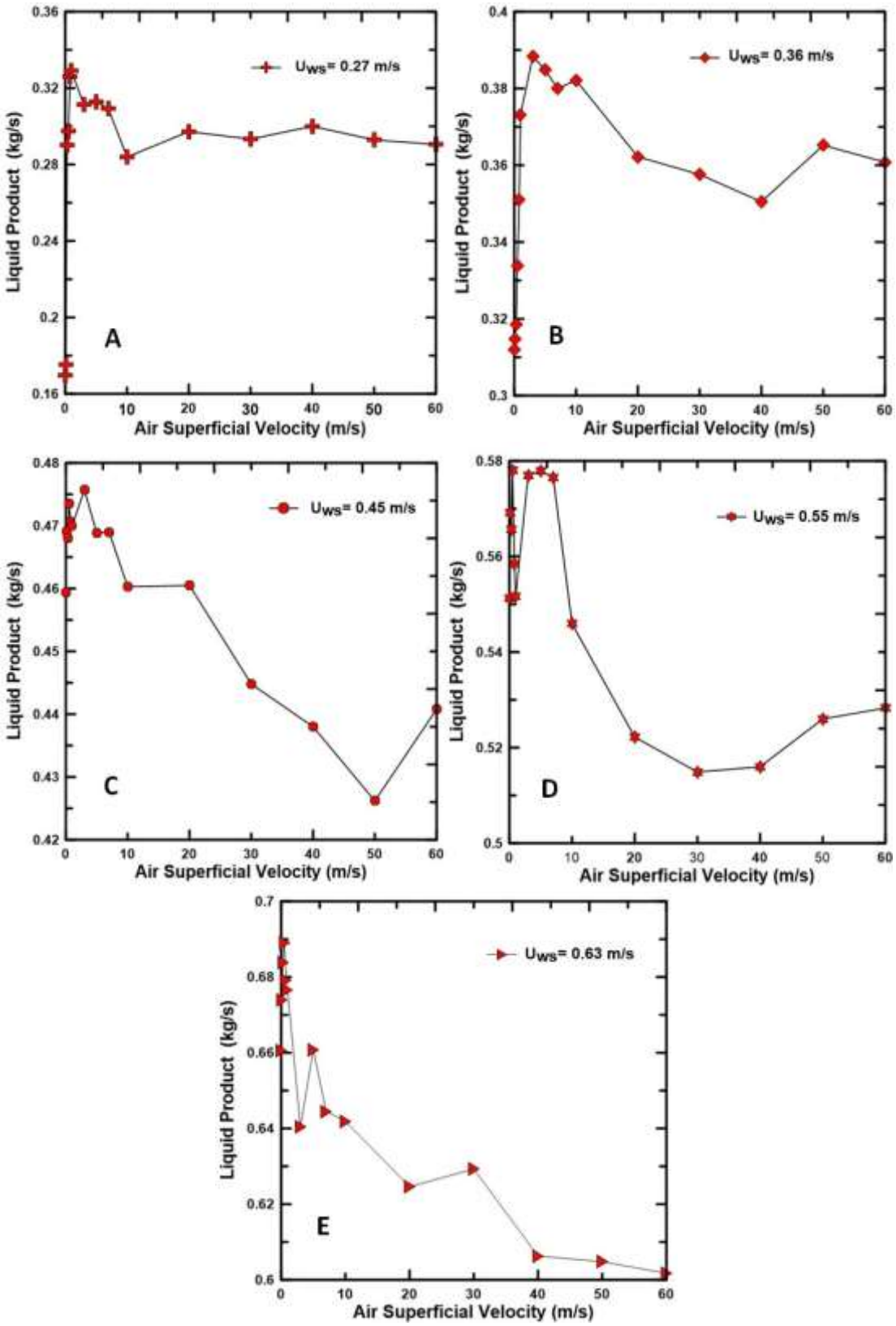

Fig. 27(A–E): The quantity of the liquid product obtained with different air superficial velocities, with the water superficial velocity kept constant

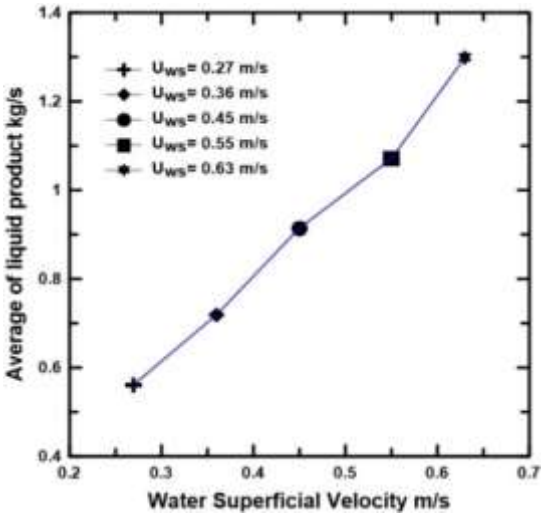

Fig. 28: Behavior of the average liquid product when increased water superficial velocities

5 Conclusion

This study investigated the relationship between pressure drop and the various flow patterns observed in perforated horizontal pipes. The predicted flow patterns included bubble flow, transition bubble/dispersed bubble flow, transition bubble/slug flow, slug flow, stratified flow, transition slug/stratified wave flow, and stratified wave flow. The impact of the friction factor was analyzed using experimental data from both unperforated and perforated pipes. Additionally, the study examined the behavior of liquid products within these flow patterns within the perforated horizontal wellbore.

Based on the Presented Experimental Results, the Following Conclusions can be drawn:

- The static pressure drop decreases with the air phase but increases with the water phase flow due to the concentration of water density.
- Transitions between flow patterns occurred with increasing superficial air velocity while maintaining constant superficial water velocity.
- Fluctuations in pressure drop were more pronounced at higher superficial air velocities and decreased with lower water holdup fractions.
- Stratified wave flow exhibited the highest peak in static pressure drop due to the significant kinetic energy of the waves in this pattern, although it also offered greater stability due to being solely influenced by the air phase.
- High holdup fractions in bubble flow patterns resulted in elevated static pressure drop values, while lower values were observed in stratified and stratified wave flow patterns due to increased void fractions.
- The quantity of liquid product increased with higher water superficial velocity, corresponding to a rise in the holdup fraction value.
- Liquid product exhibited an increase during bubble and slug flow patterns but decreased during the transition from slug and stratified flow to stratified wave flow.
- The average liquid product increased with greater mixture superficial velocity as a result of a larger water phase contribution.
- The percentage of the liquid product increased with higher water superficial velocity while maintaining constant air superficial velocity.
- While good convergence between experimental and numerical results was observed for slug and stratified flow patterns, some discrepancies in pressure drop behavior were found during the bubble, transition bubble/dispersed bubble flow, and stratified wave flow patterns.

Acknowledgement:
The authors would like to acknowledge the financial support received from the Ministry of Education Malaysia under the Fundamental Research Grant Scheme (FRGS) scheme (20180110FRGS) that enable the work to be carried out.

Nomenclature:

$f_{\circ}$	friction factor of the unperforated pipe
f	friction factor of the roughness perforation
A	universal velocity (m/s)

d	diameter of the perforations (m)
μ_m	viscosity of mixture flow $kg/m.s$
ρ_m	density of mixture flow (kg/m^3)
A_a	Area cross-section of air m^2
A_w	Area cross-section of water m^2
A_m	Area cross-section of mixture phase m^2
Re_m	Mixture Reynolds number
U_{in}	Velocity of water phase m/s
U_m	Mixture superficial velocity m/s
U_{as}	Air superficial velocity m/s
U_{ws}	Water superficial velocity m/s
n	perforation density $1/m$
Q	volume flow rate of water m^3/s
D	Diameter of mean pipe m
V_m	Mixture superficial velocity at – Y m/s
W_m	Mixture superficial velocity at – Z m/s
l	Length of the pipe m

References:

[1] Al-Wahaibi, T., Smith, M., & Angeli, P. (2007). Effect of drag-reducing polymers on horizontal oil–water flows. *Journal of Petroleum Science and Engineering*, 57(3-4), 334-346.

[2] Al-Wahaibi, T., Al-Wahaibi, Y., Al-Ajmi, A., Al-Hajri, R., Yusuf, N., Olawale, A. S., & Mohammed, I. A. (2014). Experimental investigation on flow patterns and pressure gradient through two pipe diameters in horizontal oil–water flows. *Journal of Petroleum Science and Engineering*, 122, 266-273.

[3] Razavi, S. Y., & Namin, M. M. (2011). Numerical model of slug development on horizontal two-phase flow. In *Proceedings of The International Conference on Recent Trends in Transportation, Environmental and Civil Engineering* (pp. 14-15).

[4] Pham, H., Wen, L., & Zhang, H. (2012). Numerical simulation and analysis of gas-liquid flow in a T-junction microchannel. *Advances in Mechanical Engineering*, 4, 231675.

[5] Vásquez, F., Stanko, M., Vásquez, A., De Andrade, J., & Asuaje, M. (2012). Air–water: two phase flow behavior in a horizontal pipe using computational fluids dynamics (CFD). *WIT Transactions on Engineering Sciences*, 74, 381-392.

[6] Hassanlouei, R. N., Firouzfar, H., Kasiri, N., & Khanof, M. H. (2012). A simple mathematical model for slug liquid holdup in horizontal pipes. *Scientia Iranica*, 19(6), 1653-1660.

[7] Liu, D., Ling, X., & Peng, H. (2016). Comparative analysis of gas–liquid flow in T-junction microchannels with different inlet orientations. *Advances in Mechanical Engineering*, 8(3), 1687814016637329.

[8] Santos, R. M., & Kawaji, M. (2010). Numerical modeling and experimental investigation of gas–liquid slug formation in a microchannel T-junction. *International Journal of Multiphase Flow*, 36(4), 314-323.

[9] Arias, S., Legendre, D., & González-Cinca, R. (2012). Numerical simulation of bubble generation in a T-junction. *Computers & fluids*, 56, 49-60.

[10] Shi, Y., Tang, G. H., & Xia, H. H. (2014). Lattice Boltzmann simulation of droplet formation in T-junction and flow-focusing devices. *Computers & Fluids*, 90, 155-163.

[11] Chandra, A. K., Kishor, K., Mishra, P. K., & Alam, M. S. (2016). Numerical investigations of two-phase flows through enhanced microchannels. *Chemical and Biochemical Engineering Quarterly*, 30(2), 149-159.

[12] Wong, V. L., Loizou, K., Lau, P. L., Graham, R. S., & Hewakandamby, B. N. (2017). Numerical studies of shear-thinning droplet formation in a microfluidic T-junction using two-phase level-SET method. *Chemical Engineering Science*, 174, 157-173.

[13] Vieira, R. E., Kesana, N. R., McLaury, B. S., Shirazi, S. A., Torres, C. F., Schleicher, E., & Hampel, U. (2014). Experimental investigation of the effect of 90 standard elbow on horizontal gas–liquid stratified and annular flow characteristics using dual wire-mesh sensors. *Experimental thermal and fluid science*, 59, 72-87.

[14] Qiji, S. U. N., & Xu, W. A. N. G. (2014). Horizontal Well Bottom-Hole Pressure Drop Steam Flooding Numerical Calculation. *Adv. Petrol. Explorat. Dev.*, 7(2), 76-79.

[15] Talley, J. D., Worosz, T., & Kim, S. (2015). Characterization of horizontal air–water two-phase flow in a round pipe part II: Measurement of local two-phase parameters

in bubbly flow. *International Journal of Multiphase Flow*, 76, 223-236.

[16] Hua, L., Yan, L., Xiaodong, P., Xindong, L., & Laichao, W. (2016). Pressure drop calculation models of wellbore fluid in perforated completion horizontal wells. *IJHT, International Journal of Heat and Technology*, 34(1), 65-72.

[17] Morshed, M., Amin, A., Rahman, M. A., & Imtiaz, S. (2016, July). Experimental and computational analysis of pressure response in a multiphase flow loop. In *AIP Conference Proceedings* (Vol. 1754, No. 1). AIP Publishing.

[18] Hon, L. T., & Pao, W. (2017). *CFD Simulation of Two-phase Slug Flow Liquid Carryover in T-junction Corresponds to Various Diameter Ratio*. UTP Technical Report. DOI: 10.13140/RG. 2.2. 20419.20008.

[19] Sun, F., Yao, Y., Li, X., Zhao, L., Ding, G., & Zhang, X. (2017). The mass and heat transfer characteristics of superheated steam coupled with non-condensing gases in perforated horizontal wellbores. *Journal of Petroleum Science and Engineering*, 156, 460-467.

[20] Azadi, M., Aminossadati, S. M., & Chen, Z. (2016). Large-scale study of the effect of wellbore geometry on integrated reservoir-wellbore flow. *Journal of Natural Gas Science and Engineering*, 35, 320-330.

[21] Hamad, F. A., Faraji, F., Santim, C. G. S., Basha, N., & Ali, Z. (2017). Investigation of pressure drop in horizontal pipes with different diameters. *International Journal of Multiphase Flow*, 91, 120-129.

[22] Baghernejad, Y., Hajidavalloo, E., Zadeh, S. M. H., & Behbahani-Nejad, M. (2019). Effect of pipe rotation on flow pattern and pressure drop of horizontal two-phase flow. *International Journal of Multiphase Flow*, 111, 101-111.

[23] Wen, J., Yang, M., Qi, W., Wang, J., Yuan, Q., & Luo, W. (2018). Experimental analysis and numerical simulation of variable mass flow in horizontal wellbore. *International Journal of Heat & Technology*, 36(1).

[24] Hasanain. et al. (2017). "Numerical Analysis of Two-Phase Flow Patterns in Vertical and Horizontal Pipes." *Wseas Transactions on Fluid Mechanics,* 12, 131-140.

[25] Abdulkadir, M. (2011). *Experimental and computational fluid dynamics (CFD) studies of gas-liquid flow in bends*, University of Nottingham. PhD, thesis.

[26] Versteeg, H. K., & Malalasekera, W. (2007). *An introduction to computational fluid dynamics: the finite volume method*. Pearson education.

[27] Ortiz-Vidal, L. E., Mureithi, N., & Rodriguez, O. M. H. (2014). Two-phase friction factor in gas-liquid pipe flow. *Revista de Engenharia Térmica*, *13*(2), 81-88.

Contribution of Individual Authors to the Creation of a Scientific Article (Ghostwriting Policy)

The authors equally contributed to the present research, at all stages from the formulation of the problem to the final findings and solution.

Sources of Funding for Research Presented in a Scientific Article or Scientific Article Itself.

The authors would like to acknowledge the financial support received from the Ministry of Education Malaysia under the Fundamental Research Grant Scheme (FRGS) scheme (20180110FRGS) that enable the work to be carried out.

Conflict of Interest

Please check the following as appropriate:

- All authors have participated in (a) conception and design, or analysis and interpretation of the data; (b) drafting the article or revising it critically for important intellectual content; and (c) approval of the final version.
- This manuscript has not been submitted to, nor is under review at, another journal or other publishing venue.
- The authors have no affiliation with any organization with a direct or indirect financial interest in the subject matter discussed in the manuscript
- The authors have affiliations with organizations with direct or indirect financial interest in the subject matter discussed in the manuscript: